

# Shrinkage-mediated imaging of entire organs and organisms using uDISCO

Chenchen Pan<sup>1,2,6</sup>, Ruiyao Cai<sup>1,2,6</sup>, Francesca Paola Quacquarelli<sup>1,6</sup>, Alireza Ghasemigharagoz<sup>1</sup>, Athanasios Lourbopoulos<sup>1</sup>, Paweł Matryba<sup>1,5</sup>, Nikolaus Plesnila<sup>1-3</sup>, Martin Dichgans<sup>1-4</sup>, Farida Hellal<sup>1,3</sup> & Ali Ertürk<sup>1-3</sup>

**Recent tissue-clearing approaches have become important alternatives to standard histology approaches. However, light scattering in thick tissues and the size restrictions on samples that can be imaged with standard light-sheet microscopy pose limitations for analyzing large samples such as an entire rodent body. We developed ‘ultimate DISCO’ (uDISCO) clearing to overcome these limitations in volumetric imaging. uDISCO preserves fluorescent proteins over months and renders intact organs and rodent bodies transparent while reducing their size up to 65%. We used uDISCO to image neuronal connections and vasculature from head to toe over 7 cm and to perform unbiased screening of transplanted stem cells within the entire body of adult mice. uDISCO is compatible with diverse labeling methods and archival human tissue, and it can readily be used in various biomedical applications to study organization of large organ systems throughout entire organisms.**

Until recently, histological techniques relied on sectioning to observe nonsuperficial cellular structures deep in tissues. However, investigation of complex cells with large projections, such as those in the nervous system, is best performed in intact tissue. While recently developed tissue-clearing methods have overcome obstacles imposed by light scattering<sup>1-10</sup>, the difficulties associated with specimen size remain to be addressed. Available clearing methods either increase or do not change the volume of tissues, with the exception of organic-solvent-based methods such as 3D imaging of solvent-cleared organs (3DISCO), which causes a substantial volumetric reduction instead<sup>5,6,11</sup>.

When combined with tissue clearing, light-sheet microscopy produces micrometer-resolution image volumes of large specimens within minutes. However, several limitations still exist. Photons traveling through samples (cleared or uncleared) are absorbed or scattered by interaction with the tissue, resulting in attenuation of both excitation and emission light<sup>12,13</sup>. Relatively thick light sheets (thickness  $\geq 4 \mu\text{m}$ ) are used to image volumes larger than a few hundred micrometers<sup>14</sup>. These light sheets are generated by cylindrical lenses and have Gaussian profiles;

thinnest widths, which provide the best resolution, occur only at the beam waist. Thus, the volume of sample that can be imaged at the highest resolution is limited to the central region of the light sheet. Finally, both small imaging chambers and the short working distance ( $\text{WD} \leq 8 \text{ mm}$ ) of high numerical aperture ( $\text{NA} \geq 0.9$ ) objectives pose additional challenges. Thus, 3D reconstruction of neuronal connections over 5–8 mm (the approximate size of a mouse brain) has remained a challenging task.

Organic-solvent-based clearing methods, such as 3DISCO, achieve the highest level of transparency and size reduction among all clearing approaches<sup>11,15</sup>. 3DISCO has been used to study immune cells<sup>16</sup>, stem cells<sup>17</sup>, cancer cells<sup>18</sup>, and transdifferentiating lung cells<sup>19</sup>; and it has been combined with deep-tissue antibody labeling and automated activity mapping<sup>20-22</sup>. However, 3DISCO quickly quenches endogenously expressed fluorescent proteins (with a half-life of a few days)<sup>6</sup>, which has limited the applicability of 3DISCO. Here, we developed uDISCO, a method that revealed and preserved the signal of endogenous fluorescence over months while retaining the advantageous size reduction. Thus, uDISCO allows subcellular imaging of  $2\times$  to  $3\times$  larger volumes in a single scan and avoids or reduces artifacts of physical sectioning and mosaic imaging. Using uDISCO, we imaged entire bodies of adult rodents to determine long-distance neuronal and vascular projections and spatial information on stem cell transplants (which have previously been difficult to study) at single-cell resolution.

## RESULTS

### uDISCO preserves endogenous signal and reduces volume by 65%

We reasoned that 3DISCO-induced shrinkage could be promising for imaging whole rodent bodies. However, 3DISCO resulted in a fast decline of endogenous fluorescence signal during whole-body clearing, where longer treatments with clearing solutions are required (**Supplementary Figs. 1 and 2**). To overcome this, we searched for organic compounds that preserved fluorescence while providing a potent tissue-clearing effect. Our screen

<sup>1</sup>Institute for Stroke and Dementia Research, Klinikum der Universität München, Ludwig Maximilians University of Munich (LMU), Munich, Germany.

<sup>2</sup>Graduate School of Systemic Neurosciences (GSN), Munich, Germany. <sup>3</sup>Munich Cluster for Systems Neurology (SyNergy), Munich, Germany. <sup>4</sup>German Center for Neurodegenerative Diseases (DZNE, Munich), Munich, Germany. <sup>5</sup>Current address: Department of Molecular and Cellular Neurobiology, Nencki Institute of Experimental Biology of Polish Academy of Sciences, Warsaw, Poland. <sup>6</sup>These authors contributed equally to this work. Correspondence should be addressed to A.E. (ali.ertuerk@med.uni-muenchen.de).

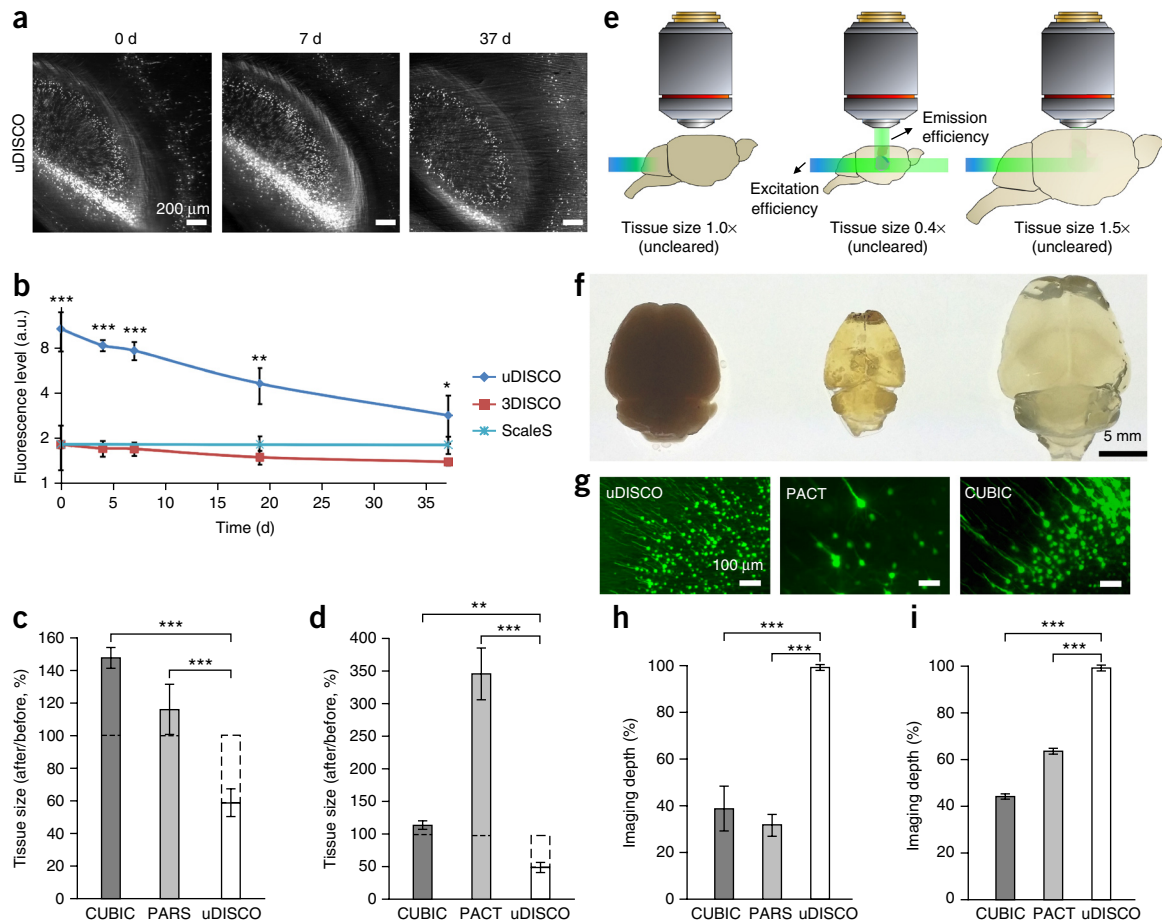


**Figure 1** | Development and principles of uDISCO. **(a)** Preservation of GFP (*Thy1*-GFP-M brain) after uDISCO, assessed by light-sheet microscopy. **(b)** Fluorescence-level quantifications in the GFP-M brains after uDISCO, ScaleS, and 3DISCO over time ( $n = 3, 3,$  and  $4$  mice, respectively; a.u., arbitrary unit). **(c)** Volume changes of 4-month-old GFP-M mice after CUBIC, PARS, and uDISCO whole-body clearing ( $n = 5, 3,$  and  $7$  mice, respectively). **(d)** Volume changes of dissected brains from 6-month-old mice after CUBIC, PACT, and uDISCO passive clearing ( $n = 4, 4,$  and  $3$  mice, respectively). **(e)** Illustration of the advantages and disadvantages of tissue shrinkage versus expansion during imaging. **(f)** Mouse brains (GFP-M, 4 months old): uncleared (left), after uDISCO (middle), and after CUBIC (right) whole-body clearing. **(g)** Light-sheet microscopy imaging of cortical neurons in GFP-M brains with shrinkage (uDISCO) and expansion (PACT and CUBIC) after clearing. **(h)** Imaging depth quantifications on brains after CUBIC, PARS, and uDISCO whole-body clearing ( $n = 4, 4,$  and  $3$  mice, respectively). **(i)** Imaging depth quantifications on brains after CUBIC, PACT, and uDISCO passive clearing of dissected brains ( $n = 4, 3,$  and  $3$  mice (6 months old), respectively). All values are mean  $\pm$  s.d.; statistical significance in **b–d, h,** and **i** (\*,  $P < 0.05$ ; \*\*,  $P < 0.01$ ; and \*\*\*,  $P < 0.001$ ) was assessed by one-way ANOVA followed by Dunnett's *post hoc* test.

resulted in a tissue-clearing method (uDISCO) based on diphenyl ether (DPE), an organic solvent with a refractive index of 1.579 (Supplementary Fig. 3). uDISCO reveals fluorescence notably better and maintains it several weeks longer within *Thy1*-GFP-M mouse brains (expressing GFP in a sparse neuronal population<sup>23</sup>) compared with 3DISCO and water-based ScaleS protocols (Fig. 1a,b, Supplementary Figs. 4–6, and Supplementary Video 1). As DPE has a melting point of 26 °C, we mixed it with benzyl alcohol (–15 °C melting point) and benzyl benzoate (18 °C melting point) to obtain a mixture that is liquid at room temperature, which we named BABB-D (Supplementary Table 1 and Supplementary Protocol). Additionally, uDISCO utilizes both the antioxidant  $\alpha$ -tocopherol (Vitamin E) to scavenge peroxides and *tert*-butanol<sup>24</sup>, a dehydrating reagent that is more stable than tetrahydrofuran (THF) used in 3DISCO. With the resulting protocol, the fine structures of labeled neurons in the lipid-dense brain and spinal cord can be detected over weeks to months.

uDISCO effectively cleared internal organs (Supplementary Fig. 7) and hard tissues, including calcified bones (Supplementary Figs. 8–10; Supplementary Videos 2 and 3), without any additional treatment, such as decalcification with EDTA<sup>25</sup>. Bones are heavily mineralized, allowing only minimal exchange of clearing solutions. Therefore, bone clearing requires clearing solutions with similar refractive index (RI) to reduce the clearing duration and light scattering. The RI of bones has been estimated as 1.555–1.564 (refs. 26 and 27), which is very similar to the RI of BABB-D, the final clearing agent in uDISCO.

We measured the size-reduction capability of uDISCO compared with existing whole-body clearing techniques. We found that whole-body clearing by uDISCO reduced the volume of mice (~42%), while both CUBIC (clear, unobstructed brain imaging cocktails and computational analysis) and PARS (perfusion-assisted agent release *in situ*) whole-body clearing methods enlarged it (Fig. 1c and Supplementary Fig. 11). We also tested the size reduction on dissected organs and found that uDISCO

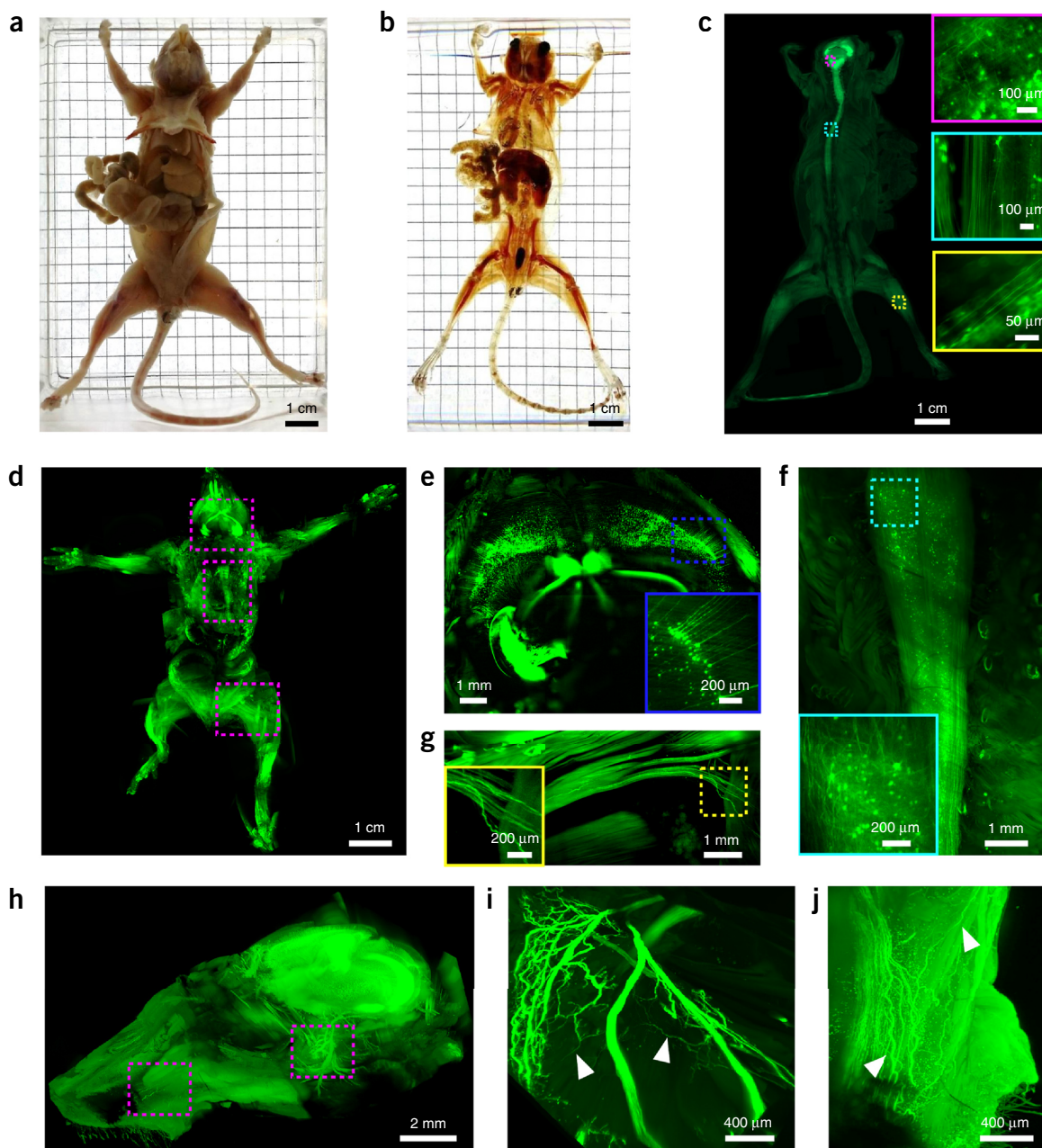


**Figure 2** | Whole-body clearing and imaging of adult mouse with uDISCO. (a–c) Adult GFP-M mouse (3 months old) was transcardially perfused (a), cleared with uDISCO (b) and imaged by fluorescence stereomicroscope at cellular resolution (c). Insets show higher-magnification images of the brain (magenta rectangle), spinal cord (cyan rectangle), and sciatic nerve (yellow rectangle). (d) Whole-body light-sheet imaging of intact GFP-M mouse (4 weeks old). (e–g) High-magnification images of the boxed regions in d. Colored rectangles show high-magnification images from the indicated regions in the brain (e), spinal cord (f), and sciatic nerve (g). (h) 3D visualization of the intact head from *Thy1*-YFP-H mouse (4 months old) after whole-body uDISCO clearing, indicating the detailed structure of optic nerve (i) and nerves at the base of the whiskers (j). The arrowheads in i and j mark some of the individual axons. The composites in c, d, and h were obtained via tile imaging.

reduced the size of adult mouse brains up to 55%, in contrast to CUBIC and PACT (passive CLARITY technique), both of which enlarged mouse brains (Fig. 1d and Supplementary Fig. 11). This size reduction, together with uDISCO's preservation of fluorescent proteins, resulted in a substantial advantage for imaging larger volumes compared with other tissue-clearing methods (Fig. 1e,f). Using light-sheet microscopy, we found that the maximum portion of a cleared tissue that can be imaged at once increased 2× to 4× with uDISCO compared with PARS or PACT and CUBIC (Fig. 1g–i).

To test whether the shrinkage was isotropic, we compared images before and after clearing. We found that brain tissues such as the cortex and hippocampal layers shrank homogeneously, ~30% in each dimension at macroscopic scale (Supplementary Fig. 12). In addition, the shrinkage of different cell types (neurons, glia, etc.) and vasculature in the same brain region was homogenous in all dimensions (Supplementary Fig. 13). Finally, we found that individual cell and vascular morphologies were preserved in brain tissue after uDISCO clearing (Supplementary Fig. 14).

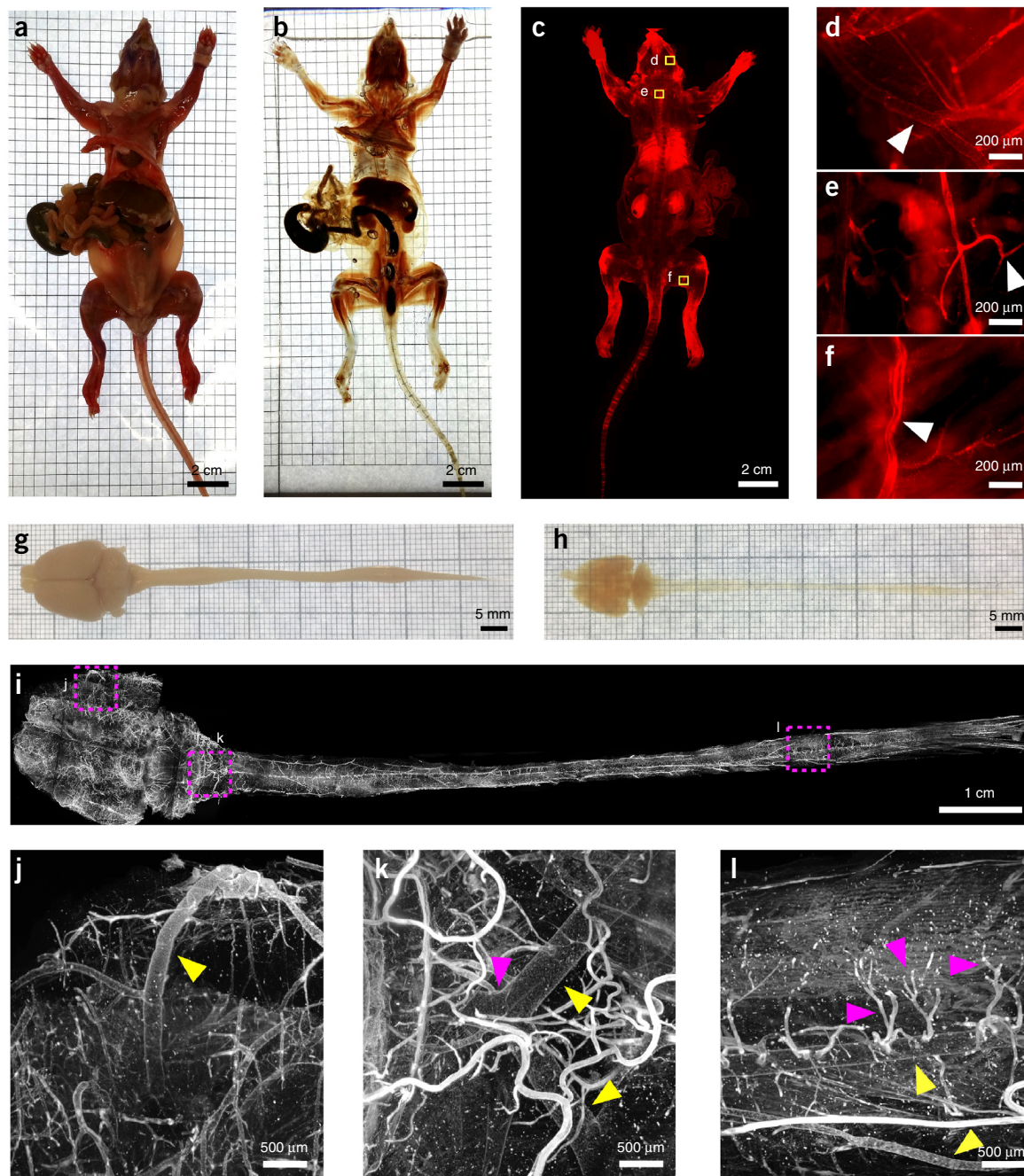


**Figure 3** | Whole-body clearing and imaging of rats with uDISCO. (a–c) A young adult female rat (4 weeks old) was injected with Texas Red Dextran to label the vasculature. The rat was transcardially perfused (a), cleared with uDISCO (b) 20 min after the dextran injection, and imaged with a fluorescence stereomicroscope (c). (d–f) High-magnification images of the boxed regions in c, such as the brain (d), spinal cord (e), and hindlimb (f). (g–i) Adult rat (10 weeks old) CNS (brain and spinal cord) before (g) and after (h) uDISCO clearing. (i–l) 3D visualization of vasculature via light-sheet imaging throughout the entire CNS from the adult rat (i). The vasculature in the cortex (j) (yellow arrowhead shows the right middle cerebral artery), brainstem (k) (yellow arrowheads show the two vertebral arteries, and purple arrowhead shows the basilar artery), and lumbar spinal cord (l) (yellow arrowheads show the spinal vessels, and purple arrowheads show their small subcal branches) are shown. The composites in c and i were obtained via tile imaging.

#### uDISCO enables micrometer-resolution whole-body imaging

We used uDISCO on whole rodent bodies for system-level interrogation. We cleared the whole body of an adult *Thy1*-GFP-M mouse within 3–4 d (Fig. 2a,b; 3-month-old mouse; the skin was removed before clearing). We first imaged the whole transparent mouse with a standard fluorescence stereomicroscope (Fig. 2c; the skull and vertebra were removed for epifluorescence

imaging). We readily identified the individual neurons and their extensions throughout the brain, spinal cord, and limbs in the intact mouse (Fig. 2c). To accommodate the entire transparent mouse into the imaging chamber of a standard light-sheet microscope, we constructed sample holders to keep the cleared specimens in place within the imaging chamber for automated tile scans without obstructing the excitation light

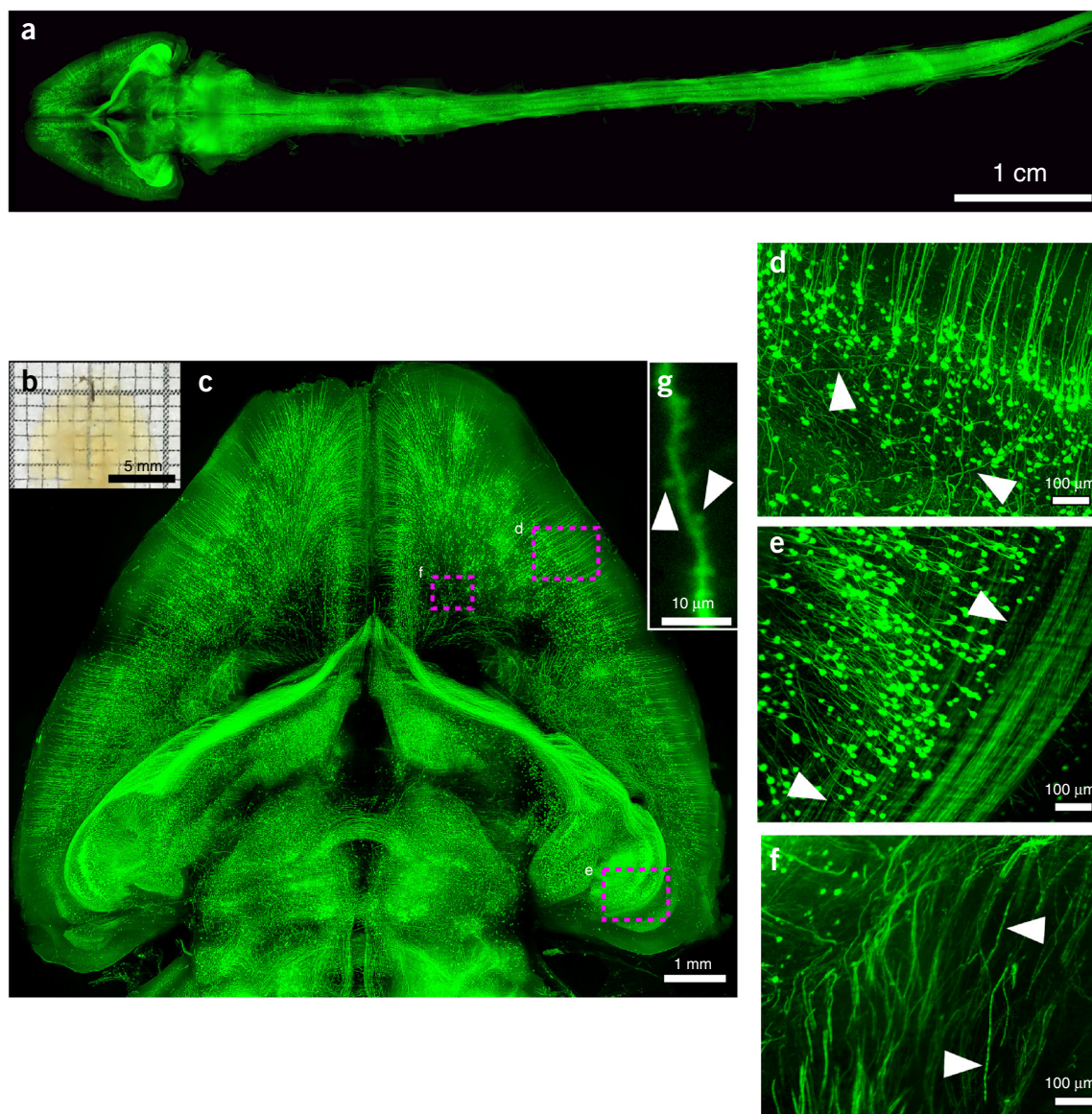


**Figure 4** | Projections throughout the entire adult mouse CNS (whole brain and spinal cord). (a) The intact CNS from a GFP-M mouse (4 months old) after uDISCO clearing and light-sheet microscopy imaging. (b) Image of the brain in **a** showing the transparency after uDISCO. (c) Details of neuronal structures in the entire brain in **a**. (d–f) High-magnification images of boxed regions in **c**, showing the neuronal structures at subcellular resolution in the cortex (d), in the hippocampus (e), and projecting to the midbrain (f). (g) After uDISCO, imaging of dendritic spines with light-sheet microscopy. The composites in **a** and **c** were obtained via tile imaging.

(**Supplementary Figs. 15 and 16**). Upon shrinkage, the width of the largest body region (torso) was reduced from  $2.24 \pm 0.052$  cm to  $2.0 \pm 0.048$  cm (mean  $\pm$  s.e.m.,  $n = 7$  mice), allowing us to complete 10-mm depth scans from dorsal and ventral sides of the mouse (**Supplementary Fig. 17**). Subsequently, we imaged the entire transparent mouse using light-sheet microscopy to detect neuronal structures throughout the intact mouse body at  $\sim 0.5$ - to  $2$ - $\mu\text{m}$  lateral and  $\sim 4$ - $\mu\text{m}$  axial resolution (**Fig. 2d**). Subcellular details of neuronal projections in the whole body were visible throughout the animal with light-sheet microscopy (**Fig. 2e–g**). In addition, large body regions such as the head, torso, and whole limbs could be studied in detail. For example, when we imaged the entire head from an adult *Thy1*-YFP-H mouse<sup>23</sup>, we observed the projections of optic nerves and innervation of whiskers (**Fig. 2h–j**).

uDISCO is also applicable to larger rodents. Rats (*Rattus norvegicus*) are valuable experimental models in toxicology and neurological studies because, compared with those of mice, rat physiology and behavior more closely resemble those of humans. uDISCO successfully cleared whole rats (**Fig. 3a,b** and **Supplementary Fig. 18**). We could observe the details of Texas Red–dextran-labeled vasculature in the brain, brainstem, and limbs using a standard fluorescence stereomicroscope in the intact 4-week-old rats (**Fig. 3c–f**). In addition, uDISCO achieved uniform clearing and over 60% tissue shrinkage of the intact central nervous system (CNS) in adult rats (10 weeks old,  $n = 4$  rats; **Fig. 3g,h**). Subsequently, we obtained light-sheet microscopy images of the vasculature in the intact CNS over 13 cm (**Fig. 3i** and **Supplementary Video 4**). We identified vascular structures such as the right middle cerebral artery (**Fig. 3j**); the two vertebral

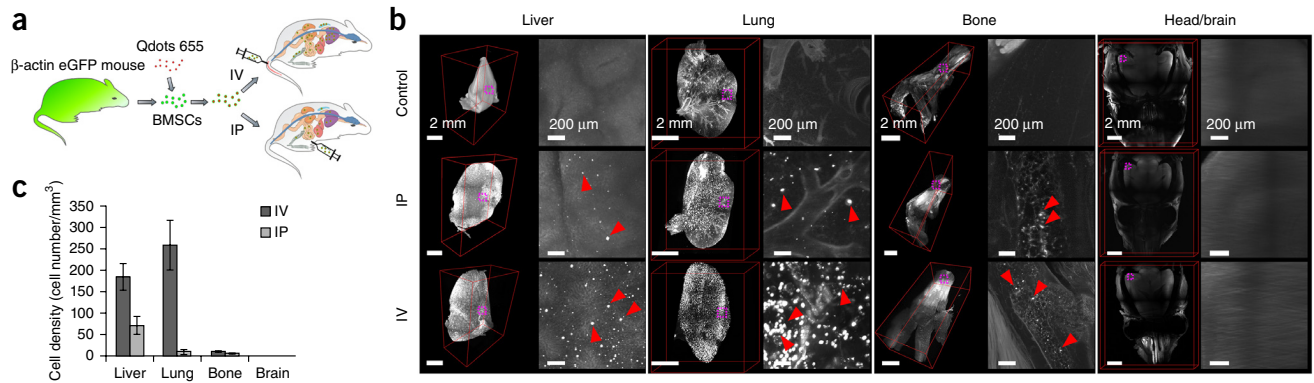


**Figure 5** | Distribution of mouse BMSCs after transplantation. **(a)** Illustration of the experimental design. **(b)** Images of liver, lung, limb, and head (brain) from host mice in control, IP, and IV groups assessed by light-sheet imaging. The composites of individual organs were obtained via tile imaging. The background autofluorescence signal outlines the overall morphology of the organs. Some Qdots-positive BMSCs are indicated by red arrowheads. **(c)** Quantification of BMSCs in different organs. Values are mean  $\pm$  s.e.m.;  $n = 3$  mice for each group (control, IP, and IV).

arteries, which merge to form the basilar artery (Fig. 3k); and the spinal vessels and their small sulcal branches (Fig. 3l).

#### uDISCO allows tracing of the intact central nervous system

Since we could image the intact CNS of rodents with light-sheet microscopy at subcellular resolution, we used uDISCO to trace neuronal structures from head to toe in the entire CNS (brain and spinal cord) of 3- to 5-month-old *Thy1-GFP-M* adult mice. We could trace individual axons in the intact CNS over several centimeters in these scans (Fig. 4a; Supplementary Videos 5 and 6). Focusing on the brain, we observed the details of neuronal structures in the cortex, the hippocampus, and fine axonal projections to the midbrain (Fig. 4b–f and Supplementary Video 7). PACT<sup>1</sup> and CUBIC<sup>8</sup> reported visualization of dendritic spines using confocal or two-photon microscopy. For the first time for an organic-solvent-based clearing method in intact adult mouse brain, uDISCO achieved dendritic-spine resolution using light-sheet microscopy (Fig. 4g and Supplementary Video 8).

#### uDISCO allows interrogation of BMSCs in the entire mouse

Bone marrow stem cells (BMSCs) are widely used for neuroprotection, regeneration, immunomodulation, and localized drug delivery studies<sup>28,29</sup>. So far, assessment of their distribution and densities has relied on methods such as histology, bioluminescence, or radiolabeling<sup>30</sup>. These approaches are time consuming and lack the sensitivity to detect sparsely localized cells or unexpected sites of grafting<sup>31</sup>. We used uDISCO whole-body clearing for an unbiased screen of transplanted syngeneic mouse BMSCs in the entire body at single-cell resolution. We collected BMSCs from  $\beta$ -actin EGFP mice as described previously<sup>32</sup> and labeled them with quantum dots (Qdots) (Supplementary Fig. 19). Cells easily incorporate Qdots, which do not interfere with cell functionality or migration capacities and therefore Qdots are widely used for cell tracking<sup>33</sup>. Subsequently, we injected the cells either intravenously (IV) or intraperitoneally (IP) into host C57BL/6N mice (Fig. 5a). Control animals were injected with vehicle (PBS) only. At 3 h after injection, we euthanized the animals for whole-body clearing. We first imaged whole mouse bodies using a fluorescence stereomicroscope to determine sites of grafted BMSCs (Supplementary Fig. 20). Subsequently, we performed high-resolution light-sheet microscopy on body parts and organs

that hosted BMSCs. As expected, the majority of BMSCs were trapped in the first-passage, low-flow organs such as the lungs, liver, and spleen after IV injection (Fig. 5b,c, Supplementary Figs. 20–22, and Supplementary Video 9)<sup>31,34</sup>. Moreover, we detected sparsely distributed BMSCs in organs such as kidneys, bone marrow, and intestines (Fig. 5b,c; Supplementary Figs. 21 and 22). The localizations in bone marrow and intestines are of high interest because they were previously difficult to investigate despite their importance for hematopoietic cell populations or immune reactions<sup>31</sup>. As reported<sup>35</sup>, we did not observe any BMSCs in the intact healthy CNS (Fig. 5b,c). Overall, our data demonstrate that uDISCO whole-body clearing can be used to study density and distribution of fluorescently labeled transplanted cells throughout the entire host body at single-cell resolution in an unbiased way, combining both high speed and resolution for transplantation studies.

#### uDISCO is compatible with virus labeling and immunostaining

Most animal models used in the laboratory, as well as human clinical samples, do not express fluorescent proteins. Hence, we sought to test alternative methods to label tissues for uDISCO. To this end, we used adeno-associated virus (AAV) tracing to label neurons in the CNS of mice. We transduced the right motor cortex of mice with AAV2-Syn-EGFP and the left motor cortex with AAV2-Syn-RFP (Fig. 6a). 4 weeks after transduction, we performed whole-body uDISCO clearing. Fluorescence expression of the virally delivered proteins was detectable in the brain and throughout the intact spinal cord (Fig. 6b–f and Supplementary Fig. 23). The pyramidal decussation of descending motor axons was clearly visible (Fig. 6c). We detected both bundles of axons as well as individual axons in the brain and spinal cord over several centimeters (Fig. 6d–f).

Antibody staining is a valuable approach for labeling molecules of interest without the need for fluorescent tagging. Deep-tissue antibody-labeling methods<sup>20,21</sup> were recently combined with 3DISCO. To test these methods with uDISCO, we cut 1-mm-thick tissue sections of mouse brains and labeled them with antibodies against glial fibrillary acidic protein (GFAP) and ionized calcium binding adaptor molecule 1 (Iba1) as well as with a DNA-specific dye (Fig. 6g). After uDISCO, the slices shrank more than 60% in volume. We found that the signals from GFAP (astrocytes), Iba1 (microglia and macrophages), and TO-PRO-3 (DNA dye) were visible

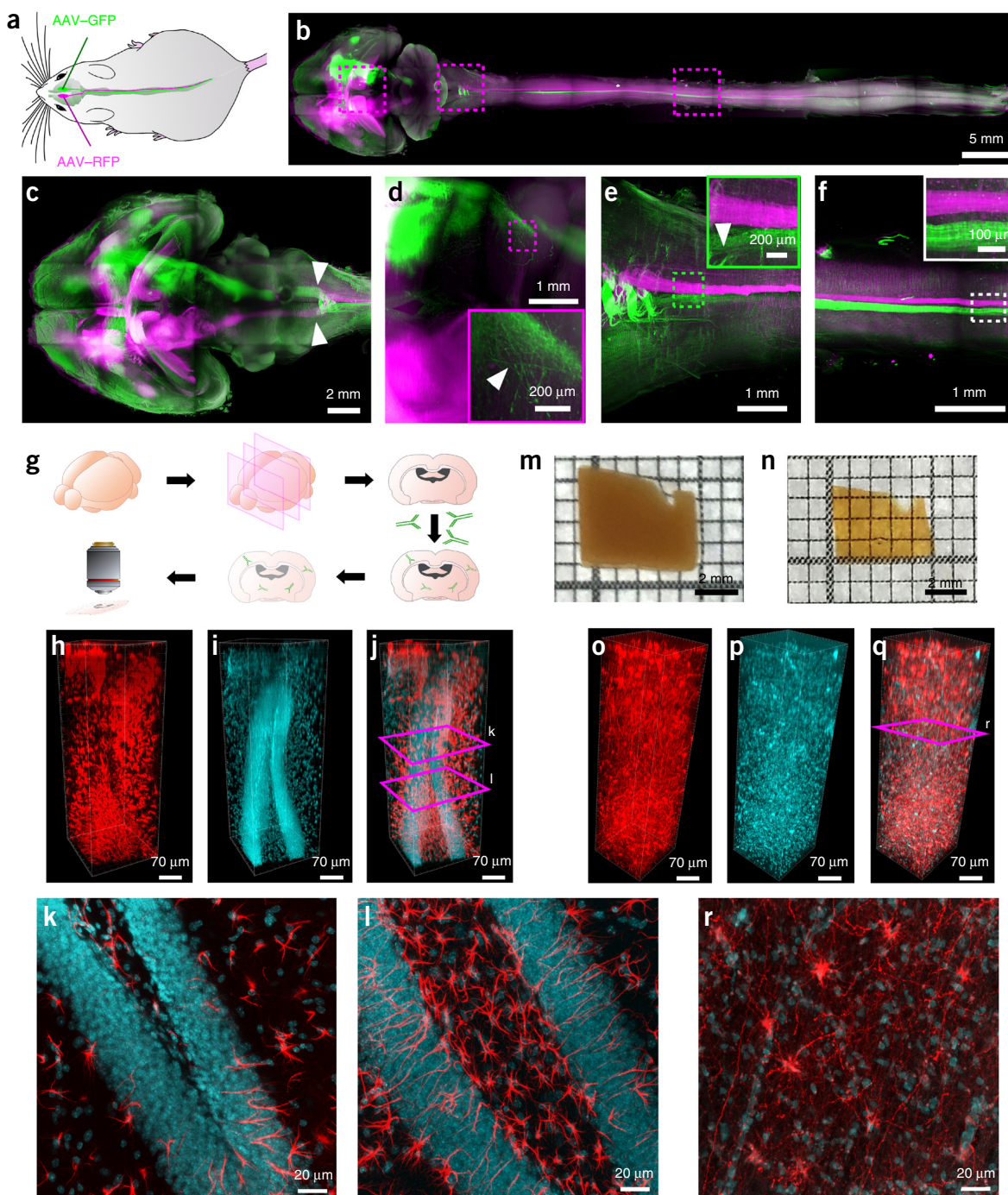


**Figure 6** | uDISCO is compatible with AAV neuron tracing and immunolabeling. **(a)** Experimental design for AAV-Syn-RFP and AAV-Syn-GFP injections. **(b,c)** Maximum-intensity projections of the entire brain **(b,c)** and CNS **(b)** after whole-body uDISCO clearing. Arrowheads in **c** indicate decussation of the descending motor axons. **(d-f)** Details of neuronal extensions of boxed regions in **(b)**: the thalamus and midbrain **(d)**, cervical **(e)**, and thoracic **(f)** spinal cord regions. Colored rectangles show the enlarged views from the respective images. **(g)** Immunolabeling workflow. **(h-l)** GFAP and TO-PRO-3 labeling of coronal sections. 3D reconstructions show labeling of astrocytes **(h)** and cell nuclei **(i)** stained by GFAP antibody and TO-PRO-3, respectively. **(j)** Merged image of **h** and **i**. **(k,l)** Maximum-intensity projections of the z-positions marked by purple boxes in **j**; nuclei are shown in cyan and astrocytes in red. **(m,n)** 14-month fixed human tissue before **(m)** and after **(n)** uDISCO. **(o-r)** GFAP and TO-PRO-3 labeling of 14-month fixed human cortical tissue. Astrocytes **(o)** and nuclei **(p)** are labeled. **(q)** Merged image of **o** and **p**. **(r)** Maximum-intensity projection of the z-position marked by the purple box in **q**; nuclei are shown in cyan and astrocytes in red. All values are mean  $\pm$  s.d. The composites in **b** and **c** were obtained via tile imaging.

throughout the tissue, indicating compatibility of uDISCO with deep-tissue labeling (**Fig. 6h–l** and **Supplementary Fig. 24**).

Human clinical tissue samples are typically stored in 4% formalin over extended periods of time. To determine whether uDISCO

could be applied to such specimens, we immunostained 1-mm-thick human samples (archived for either 1 month or 14 months) for GFAP and TO-PRO-3 or Iba1 and TO-PRO-3. We measured shrinkage of 52% and 46% in samples stored for 1 month or 14 months,

respectively (Fig. 6m,n). uDISCO allowed successful clearing, signal preservation, and imaging of human tissues stored in formalin more than a year (Fig. 6o–r and Supplementary Fig. 25), although the image quality was better for shorter storage periods (Supplementary Fig. 25i). Importantly, the combination of uDISCO and deep-tissue antibody labeling did not require additional antigen retrieval steps. Overall, these results demonstrate that uDISCO is a versatile method that can be used to clear and image different types of tissues with various labeling methods.

## DISCUSSION

uDISCO achieved whole-body clearing and imaging because of sample-size reduction and preservation of fluorescent proteins. Another major advantage of organic-solvent-based clearing methods is the easy handling of cleared tissues; specimens become hard because of dehydration, yet are flexible enough for versatile positioning of long samples, such as the entire spinal cord of adult rats. In contrast, concentrated glycerol and sugar solutions used in various clearing methods are difficult to work with because of their high viscosity, the resulting gel-like texture of the cleared tissue, and the air bubbles generated during the refractive-index matching procedures and imaging<sup>11</sup>.

Recently, tissue expansion was used to obtain super-resolution images of small volumes (expansion microscopy)<sup>36–38</sup>. Treweek *et al.*<sup>25,39</sup> used a similar concept (expansion (e) PACT) for high-resolution imaging. While expansion provides more resolution, tissue shrinkage, in theory, decreases resolution (30% in one dimension for uDISCO). However, uDISCO resulted in high-quality images (Supplementary Fig. 26), allowing the visualization of dendritic spines and individual axons over several centimeters in the intact CNS of adult mice. This high image quality could result from a larger proportion of shrunken samples (compared with nonshrinking samples) fitting into the optimal imaging region of the light sheet. Hence, shrinkage allows imaging of 2× to 3× larger volumes in the same setup without apparent loss of resolution. Importantly, uDISCO did not alter the structural integrity of the brain either at macroscopic (e.g., cortex and hippocampus structures) or microscopic scales (e.g., individual cells). However, isotropic shrinkage remains to be confirmed for other tissues such as muscle or fat. In addition, uDISCO can be combined with microscopy techniques that deliver even higher resolution and/or faster scanning, such as confocal, two-photon, and lattice light-sheet microscopy<sup>40</sup>. We demonstrated that high numerical aperture (NA), long working distance objectives such as Zeiss CLARITY 20× and Olympus 25× are compatible with uDISCO (Supplementary Fig. 27).

Acute injuries in the CNS might affect not only the injury site but also uninjured distal parts of the CNS<sup>41,42</sup>. Thus, repair strategies after CNS traumas need to be evaluated throughout the entire CNS. The uDISCO approach enables the assessment of long-range axonal projections and individual cells throughout entire organisms. Hence, this approach can help to reduce (1) the bias of analyzing only selected organs; (2) the time needed to prepare and screen individual organs and body parts of a complete mouse<sup>43</sup>; and (3) by generating whole mouse atlases and databases it can reduce the resources and number of animals needed in experimental research.

Whole-body clearing of diverse tissues, and the compatibility of this method with different imaging techniques, may have broad applications in the biomedical sciences. Whole-body clearing

approaches could facilitate the assessment of neurodegeneration in diseases that affect both the central and peripheral nerves such as in amyotrophic lateral sclerosis (ALS), inflammation that may extend from gut to brain, stem cell transplantation studies, or even 3D mapping of the cellular structures in larger brain volumes, possibly even the whole human brain.

## METHODS

Methods and any associated references are available in the [online version of the paper](#).

*Note: Any Supplementary Information and Source Data files are available in the online version of the paper.*

## ACKNOWLEDGMENTS

This work was supported by the Vascular Dementia Research Foundation, Synergy Excellence Cluster Munich (SyNergy), ERA-Net Neuron (01EW1501A to A.E. and N.P.), and the European Union's Horizon 2020 research and innovation programme (grant agreement no. 666881, SVDs@target, M.D.). A.L. and N.P. were supported by a Marie Curie Intra European Fellowship grant (FP7-PEOPLE-2013-IEF, project no. 625970). We thank M. Hübener and F. Voss (Max Planck Institute of Neurobiology, Munich) for providing mice; D. Trauner and O. Thorn-Seshold for helpful discussions; A. Weingart for illustrations; and C. Hojer, S. Tappan and T. Misgeld for critical reading of the manuscript. C.P. and R.C. are members of the Graduate School of Systemic Neurosciences (GSN), Ludwig Maximilian University of Munich. Human tissues were provided by the brain bank of the Institute of Anatomy, University of Leipzig.

## AUTHOR CONTRIBUTIONS

A.E. designed and led all aspects of the project. C.P., R.C., and F.P.Q. performed most of the experiments. A.G. performed the image rendering and developed algorithms for data analysis. C.P., R.C., F.P.Q., and A.G. analyzed the data. A.L. interpreted data and performed the BMSC cultures, characterization, and transplantations; F.H. performed virus tracing; P.M. assisted first-clearing experiments; N.P. and M.D. supervised A.L. and F.H., respectively. A.E., C.P., R.C., F.P.Q., and A.G. wrote the paper. All authors edited the paper.

## COMPETING FINANCIAL INTERESTS

The authors declare no competing financial interests.

Reprints and permissions information is available online at <http://www.nature.com/reprints/index.html>.

1. Yang, B. *et al.* Single-cell phenotyping within transparent intact tissue through whole-body clearing. *Cell* **158**, 945–958 (2014).
2. Hama, H. *et al.* ScaleS: an optical clearing palette for biological imaging. *Nat. Neurosci.* **18**, 1518–1529 (2015).
3. Chung, K. *et al.* Structural and molecular interrogation of intact biological systems. *Nature* **497**, 332–337 (2013).
4. Tainaka, K. *et al.* Whole-body imaging with single-cell resolution by tissue decolorization. *Cell* **159**, 911–924 (2014).
5. Ertürk, A. *et al.* Three-dimensional imaging of the unsectioned adult spinal cord to assess axon regeneration and glial responses after injury. *Nat. Med.* **18**, 166–171 (2011).
6. Ertürk, A. *et al.* Three-dimensional imaging of solvent-cleared organs using 3DISCO. *Nat. Protoc.* **7**, 1983–1995 (2012).
7. Kuwajima, T. *et al.* ClearT: a detergent- and solvent-free clearing method for neuronal and non-neuronal tissue. *Development* **140**, 1364–1368 (2013).
8. Susaki, E.A. *et al.* Whole-brain imaging with single-cell resolution using chemical cocktails and computational analysis. *Cell* **157**, 726–739 (2014).
9. Ke, M.T., Fujimoto, S. & Imai, T. SeedB: a simple and morphology-preserving optical clearing agent for neuronal circuit reconstruction. *Nat. Neurosci.* **16**, 1154–1161 (2013).
10. Susaki, E.A. *et al.* Advanced CUBIC protocols for whole-brain and whole-body clearing and imaging. *Nat. Protoc.* **10**, 1709–1727 (2015).
11. Richardson, D.S. & Lichtman, J.W. Clarifying tissue clearing. *Cell* **162**, 246–257 (2015).
12. Tuchin, V.V. Tissue optics and photonics: light-tissue interaction. *Journal of Biomedical Photonics & Engineering* **1**, 98–134 (2015).
13. Lichtman, J.W. & Conchello, J.A. Fluorescence microscopy. *Nat. Methods* **2**, 910–919 (2005).

14. Dodt, H.U. *et al.* Ultramicroscopy: three-dimensional visualization of neuronal networks in the whole mouse brain. *Nat. Methods* **4**, 331–336 (2007).
15. Susaki, E.A. & Ueda, H.R. Whole-body and whole-organ clearing and imaging techniques with single-cell resolution: toward organism-level systems biology in mammals. *Cell Chem. Biol.* **23**, 137–157 (2016).
16. Liu, Z. *et al.* Immune homeostasis enforced by co-localized effector and regulatory T cells. *Nature* **528**, 225–230 (2015).
17. Espinosa-Medina, I. *et al.* Neurodevelopment. Parasympathetic ganglia derive from Schwann cell precursors. *Science* **345**, 87–90 (2014).
18. Oshimori, N., Orian, D. & Fuchs, E. TGF- $\beta$  promotes heterogeneity and drug resistance in squamous cell carcinoma. *Cell* **160**, 963–976 (2015).
19. Lafkas, D. *et al.* Therapeutic antibodies reveal Notch control of transdifferentiation in the adult lung. *Nature* **528**, 127–131 (2015).
20. Renier, N. *et al.* iDISCO: a simple, rapid method to immunolabel large tissue samples for volume imaging. *Cell* **159**, 896–910 (2014).
21. Belle, M. *et al.* A simple method for 3D analysis of immunolabeled axonal tracts in a transparent nervous system. *Cell Rep.* **9**, 1191–1201 (2014).
22. Renier, N. *et al.* Mapping of brain activity by automated volume analysis of immediate early genes. *Cell* **165**, 1789–1802 (2016).
23. Feng, G. *et al.* Imaging neuronal subsets in transgenic mice expressing multiple spectral variants of GFP. *Neuron* **28**, 41–51 (2000).
24. Schwarz, M.K. *et al.* Fluorescent-protein stabilization and high-resolution imaging of cleared, intact mouse brains. *PLoS One* **10**, e0124650 (2015).
25. Treweek, J.B. *et al.* Whole-body tissue stabilization and selective extractions via tissue-hydrogel hybrids for high-resolution intact circuit mapping and phenotyping. *Nat. Protoc.* **10**, 1860–1896 (2015).
26. Ascenzi, A. & Fabry, C. Technique for dissection and measurement of refractive index of osteones. *J. Biophys. Biochem. Cytol.* **6**, 139–142 (1959).
27. Genina, E.A., Bashkatov, A.N. & Tuchin, V.V. Optical clearing of cranial bone. *Adv. Opt. Technol.* **2008**, 1–8 (2008).
28. De Miguel, M.P. *et al.* Immunosuppressive properties of mesenchymal stem cells: advances and applications. *Curr. Mol. Med.* **12**, 574–591 (2012).
29. D'souza, N. *et al.* Mesenchymal stem/stromal cells as a delivery platform in cell and gene therapies. *BMC Med.* **13**, 186 (2015).
30. Guenoun, J. *et al.* *In vivo* quantitative assessment of cell viability of gadolinium or iron-labeled cells using MRI and bioluminescence imaging. *Contrast Media Mol. Imaging* **8**, 165–174 (2013).
31. Leibacher, J. & Henschler, R. Biodistribution, migration and homing of systemically applied mesenchymal stem/stromal cells. *Stem Cell Res. Ther.* **7**, 7 (2016).
32. Nemeth, K., Mayer, B., Sworder, B.J., Kuznetsov, S.A. & Mezey, E. A practical guide to culturing mouse and human bone marrow stromal cells. *Curr. Protoc. Immunol.* **102**, Unit 22F.12 (2013).
33. Rosen, A.B. *et al.* Finding fluorescent needles in the cardiac haystack: tracking human mesenchymal stem cells labeled with quantum dots for quantitative *in vivo* three-dimensional fluorescence analysis. *Stem Cells* **25**, 2128–2138 (2007).
34. Goldmacher, G.V. *et al.* Tracking transplanted bone marrow stem cells and their effects in the rat MCAO stroke model. *PLoS One* **8**, e60049 (2013).
35. Detante, O. *et al.* Intravenous administration of 99mTc-HMPAO-labeled human mesenchymal stem cells after stroke: *in vivo* imaging and biodistribution. *Cell Transplant.* **18**, 1369–1379 (2009).
36. Chen, F., Tillberg, P.W. & Boyden, E.S. Optical imaging. Expansion microscopy. *Science* **347**, 543–548 (2015).
37. Chozinski, T.J. *et al.* Expansion microscopy with conventional antibodies and fluorescent proteins. *Nat. Methods* **13**, 485–488 (2016).
38. Chen, F. *et al.* Nanoscale imaging of RNA with expansion microscopy. *Nat. Methods* **13**, 679–684 (2016).
39. Treweek, J.B. & Gradinaru, V. Extracting structural and functional features of widely distributed biological circuits with single cell resolution via tissue clearing and delivery vectors. *Curr. Opin. Biotechnol.* **40**, 193–207 (2016).
40. Chen, B.C. *et al.* Lattice light-sheet microscopy: imaging molecules to embryos at high spatiotemporal resolution. *Science* **346**, 1257998 (2014).
41. Bareyre, F.M. *et al.* The injured spinal cord spontaneously forms a new intraspinal circuit in adult rats. *Nat. Neurosci.* **7**, 269–277 (2004).
42. Wahl, A.S. *et al.* Neuronal repair. Asynchronous therapy restores motor control by rewiring of the rat corticospinal tract after stroke. *Science* **344**, 1250–1255 (2014).
43. Reinhardt, R.L., Khoruts, A., Merica, R., Zell, T. & Jenkins, M.K. Visualizing the generation of memory CD4 T cells in the whole body. *Nature* **410**, 101–105 (2001).

#### EDITORIAL SUMMARY

**AOP:** uDISCO clearing renders whole animals transparent and capitalizes on shrinkage to image them. This method allows the analysis of intact nervous systems and whole-body screens for transplanted cells and human tissue samples after prolonged storage.

## ONLINE METHODS

A step-by-step protocol for uDISCO is available as **Supplementary Protocol** (and ref. 44).

**Animals.** We used the following animals in the study: 1- to 6-months-old, mixed gender 27 (15 male and 12 female) C57BL/6N (Charles Rivers Laboratories), 57 (28 male and 29 female) *Thy1*-GFP mice (line GFP-M), 5 (2 male and 3 female) *Thy1*-YFP mice (line YFP-H)<sup>23</sup>, 32 (13 male and 19 female) CX3CR1-GFP mice (B6.129P-Cx3cr1tm1Litt/J), Jackson Laboratory strain code: 005582), 6 (3 male and 3 female)  $\beta$ -actin EGFP mice (C57BL/6-Tg(CAG-EGFP); 131Os/LeySopJ, Jackson Laboratory strain code: 006567), and four rats (4 female) (CD IGS Rat strain 001). Sample sizes were chosen based on preliminary experiments. Sample sizes are specified in figure legends. The animals used in this study were selected for each experiment based on their genetic background (wild type or fluorescent transgenes), and animals that resulted fluorescent-protein negative by genotyping were excluded from the study. Within each strain, animals were randomly selected; different stages of experiments (clearing, imaging, and data analysis) were carried out by different operators. Animals were housed in our animal facility under a 12/12 h light/dark cycle and were provided food and water ad libitum. Experiments were conducted according to institutional guidelines of the Ludwig Maximilian University of Munich after approval of the Ethical Review Board of the Government of Upper Bavaria (Regierung von Oberbayern, Munich, Germany). All data are reported according to the ARRIVE criteria<sup>45</sup>.

**Human tissue.** Human tissues used for this study were obtained from five donors of 64–89 years old (1 male and 4 females). Human tissue donors gave their informed and written consent to the donation of their bodies for teaching and research purposes regulated by the Saxonian Death and Funeral Act of 1994 (third section, paragraph 18 item 8).

**Perfusion and tissue preparation.** Animals were deeply anesthetized by intraperitoneal injection with the triple combination of midazolam/medetomidine/fentanyl (MMF) (1 ml per 100 g of body mass for mice) before intracardial perfusion. Subsequently, animals were perfused transcardially (100–125 mm Hg pressure on Leica perfusion one system) with heparinized 0.1 M PBS (10 U/ml of heparin, Ratiopharm) for 5–10 min at room temperature until the blood was washed out and with 4% paraformaldehyde in 0.1 M PBS (pH 7.4; Morphisto, 11762.01000) for 20 min using 100–125 mm Hg pressure. The dissected tissue samples (whole brain, spinal cord, whole brain with the spinal cord, and femurs) were postfixed in 4% paraformaldehyde for 1–2 d at 4 °C. Then, tissues were washed once in PBS for 5 min; meninges were removed; and bent samples, such as spinal cords, were kept straight for the clearing procedure.

For cut bone clearing, femurs dissected from CX3CR1-GFP mice were fixed in cold 4% PFA for 24 h. Afterwards, the bones were washed with PBS and incubated in 30% sucrose PBS solution overnight at 4 °C. For longitudinal dissection, a Leica cryostat (Leica, CM3050S) was used to cut the bones embedded in optimum cutting temperature (O.C.T.) formulation (SAKURA, 4583). The section thickness was set at 30  $\mu$ m, and the serial sectioning was performed until the entire bone marrow appeared. The

remaining intact half bones were collected and washed with PBS to remove OCT and then processed for immunostaining and respective clearing<sup>46</sup>.

For whole-body clearing, after the mouse body was well perfused and fixed, the skin was separated from the body while avoiding adhesion of pelage. The skull and vertebra were carefully opened, avoiding any damage such as puncturing and squeezing of the tissue. Whole-body tissue clearing was started immediately.

**Immunostaining.** The following antibodies and dyes were used in this study: Iba1 (Wako, 019-19741, dilution 1:350), GFAP (Dako, Z033401-2, dilution 1:350), Collagen 4 (SouthernBiotech, 1340-01, dilution 1:650), AlexaFluor 647 conjugated anti-GFP rabbit polyclonal antibody (Life Technology, A31852, dilution 1:500), TO-PRO-3 iodide (642/661) (Life Technologies, T3605, dilution 1:500), AlexaFluor 568 goat anti-rabbit IgG (H+L) (Life Technologies, A-11036, dilution 8  $\mu$ g/mL), AlexaFluor 647 goat anti-rabbit IgG (H+L) (Life Technologies, A-21245, dilution 8  $\mu$ g/mL), and Cy3 AffiniPure donkey anti-goat IgG (H+L) (Jackson, 705-165-147, dilution 1:300).

For immunostaining, the tissues (mouse brains or human tissue) were cut into 1 mm slices using a vibratome (Leica, VT1200S). Mouse sections were immunostained using iDISCO<sup>20</sup> or Belle *et al.*<sup>21</sup> protocols. We used the following iDISCO protocol. The sections were initially pretreated: first, they were washed in 0.1 M PBS for 50 min two times, then they were incubated in 50% and 80% methanol (in 0.1 M PBS) for 50 min at each step and then in 100% methanol for 1 h two times. Sections were bleached with ice-cold 5% H<sub>2</sub>O<sub>2</sub> (Sigma, D216763) and 20% DMSO (Sigma D8418)/methanol (AppliChem, 141091.1211) at 4 °C overnight. After bleaching, sections were washed in methanol for 45 min three times; then in 20% DMSO/methanol for 45 min two times; then in 80% and 50% methanol for 45 min each step; then in 0.1 M PBS for 45 min two times; and finally in PBS/0.2% Triton X-100 (Sigma, T8787) for 45 min two times. For the immunostaining step, pretreated sections were incubated in PBS–0.2% Triton X-100–20% DMSO–0.3 M glycine (Sigma, G8898) at 37 °C overnight, then blocked in PBS–0.2% Triton X-100–10% DMSO–6% goat serum at 37 °C for 1 d, washed in PBS–0.2% Tween-20 (Sigma, P9416) with 10 mg/ml heparin (PTwH) overnight and then incubated with primary antibody dilutions in PTwH–5% DMSO–3% goat serum at 37 °C with gentle shaking on an oscillator for 6–8 d, refreshing the primary antibodies once after 3–4 d. Sections were then washed for 1 h with PTwH four times and then incubated with secondary antibodies diluted in PTwH–3% goat serum at 37 °C with gentle shaking on an oscillator for 3–4 d, refreshing once after 2 d. Sections were finally washed in PTwH 30 min five times and incubated with TO-PRO-3 iodide (642w/661) (dilution 1:750) in PTwH for 5 h at room temperature with gentle oscillation, washed again for 1 h four times with PTwH, and stored at 4 °C in 0.1 M PBS until clearing.

Human sections were immunostained using a modification of the protocol from Belle *et al.*<sup>21</sup>; briefly, 1 mm thick brain sections were incubated on a rocker (IKA, 2D digital) at room temperature in PBSGT solution, which consists of 0.1 M PBS with 0.2% porcine skin gelatin (Sigma, G2500), 0.5% Triton X-100, and 0.05% sodium azide (Sigma, 71290) for 24 h. Next, PBSGT was exchanged with PBSGT + 1% goat serum containing the primary antibodies and left in incubation at 37 °C with gentle shaking on

an oscillator (IKA, MS 3 basic) for 8–9 d. The primary antibodies were refreshed once after 4–5 d. Then, samples were washed for 30 min with PBSGT five times at room temperature and incubated with secondary antibodies, diluted in PBSGT + 1% goat serum at 37 °C with gentle shaking on an oscillator for 4–5 d. The secondary antibody was refreshed once after 2 d. Finally, samples were washed for 30 min three times with PBSGT, incubated with TO-PRO-3 in PBSGT for 5 h at room temperature with gentle oscillation, washed again for 1 h four times with PBSGT and stored at 4 °C in 0.1 M PBS until clearing.

For cut bone immunostaining, collected half bones were pre-treated with 5 d of PBSGT incubation at room temperature. Then, the tissue was incubated in PBSGT with 1% goat serum and AlexaFluor 647 conjugated anti-GFP antibody (dilution 1:500) at 37 °C for 10 d, refreshing once after 5 d, and finally washed five times with PBSGT for 10 min.

**Preparation of uDISCO solutions.** Dehydrating solutions were prepared by mixing *tert*-butanol (Sigma, 360538) and distilled water in the following concentrations: 30 vol% *tert*-butanol, 50 vol% *tert*-butanol, 70 vol% *tert*-butanol, 80 vol% *tert*-butanol, 90 vol% *tert*-butanol, 96 vol% *tert*-butanol. Pure (100%) *tert*-butanol has a melting point between 23 °C and 26 °C; therefore, we recommend keeping it above the melting temperature before use. Delipidation solution dichloromethane (DCM) (Sigma, 270997) was used as a pure solution. Three refractive index matching solutions were used: BABB-D4, prepared by mixing BABB (benzyl alcohol + benzyl benzoate 1:2, Sigma, 24122 and W213802) with diphenyl ether (DPE) (Alfa Aesar, A15791) at a ratio of 4:1 and adding 0.4% vol DL- $\alpha$ -tocopherol (Vitamin E) (Alfa Aesar, A17039); BABB-D10, prepared by mixing BABB with DPE at a ratio of 10:1 and adding 0.4% vol vitamin E; BABB-D15, prepared by mixing BABB with DPE at a ratio of 15:1 and adding 0.4% vol vitamin E. In passive clearing, BABB-D4 preserved the fluorescence signal better, while BABB-D15 gave better transparency. BABB-D10 was used for whole-body tissue clearing. The ratio of DPE to BABB can be adjusted to achieve either better preservation of fluorescence or more tissue transparency.

**uDISCO passive clearing procedure.** All incubation steps were performed in a fume hood with gentle rotation or shaking using 5 ml tubes (Eppendorf, 0030 119.401) for whole mouse brain or smaller samples, or steps were performed using glass chambers (Omnilab, 5163279) for bigger samples such as rat tissues or whole brain and spinal cord. The samples were covered with aluminum foil to keep them in dark.

The clearing consisted of serial incubations of the fixed samples in 5–80 ml of 30 vol%, 50 vol%, 70 vol%, 80 vol%, 90 vol%, 96 vol% and 100% *tert*-butanol at 34–35 °C to dehydrate the tissue, followed by immersion in DCM for 45–60 min at room temperature to remove the lipids. Eventually, they were incubated in BABB-D at room temperature for at least 2 h until samples became transparent. The requirement of DCM step and the incubation time of each step in *tert*-butanol solutions depended on sample size. For instance, small tissues such as mouse spinal cord or 1-mm-thick coronal slices did not need DCM step and required short incubation times (2–4 h) per each *tert*-butanol step compared with thicker or mineralized tissues such as whole brain and intact bones (12 h). Details of each protocol are showed in

**Supplementary Table 1.** Samples could be stored in BABB-D at room temperature in dark for weeks.

All other clearing methods, including PACT, CUBIC, 3DISCO, 1-propanol BABB, ScaleS, SeeDB and Murray's clear (Fig. 1; Supplementary Figs. 5,6, and 9–11), the clearing protocols were performed following the original publications<sup>1,2,6,9,10,14,24,25,47</sup>.

**uDISCO whole-body clearing procedure.** We established a transcardial circulatory system comprised of a peristaltic pump (Gilson, Peristaltic Pump MINIPULS 3; Supplementary Fig. 28; see also the step-by-step protocol of uDISCO in Supplementary Protocol). In principle, two channels from the pump were required for circulation. The first channel pumped the clearing solution through the mouse body, and the second channel collected the solution exiting the mouse body and recirculated it back to the original bottle. Since clearing solutions are corrosive, Viton reference tubing was chosen (Gilson, F1817745) because it is resistant to clearing chemicals. First, the reference tubing was set up following the instructions, and each end of the tubing was connected to a tubing connector (Omnilab, 5434482). Next, the tubing connectors were linked with additional PVC tubing (Omnilab, 5437920). For the outflow tubing of the first channel, which injected the solution into the heart, the head part cut from a 1 ml syringe (Braun, 9166017V) was inserted as the connector of the perfusion needle and fixed with a mouse transcardiac perfusion needle (Leica, 39471024). Meanwhile, the inflow tubing of the second channel, which recirculated solution, was fixed to the glass chamber containing the mouse body. Eventually, the inflow tubing of the first channel was kept below the surface of the solution, and the circulation was started until air bubbles were pushed out from the tubing system.

All clearing steps should be performed in a fume hood. First, the mouse body was put in a glass chamber, and the perfusion needle was set into the heart through the same pinhole made during tissue preparation in the perfusion setup. Next, the chamber was covered with aluminum foil, and the transcardial circulation was started. Each gradient of dehydration solution was circulated at 8–10 ml/min for 10–12 h. As the melting point of *tert*-butanol is 23 to 26 °C (close to room temperature), a heating plate with 35–40 °C was used for the two rounds of 100% *tert*-butanol circulation to prevent the solution from solidification. The final step of tissue clearing could normally be achieved by circulating BABB-D10 with the same injection rate for 6–12 h. The transparency of the mouse body was checked by eye during clearing. Bubbles were carefully prevented from forming, especially in the first channel, at every step. For rat whole-body clearing, a thicker perfusion needle (Leica, 39471022) without rubber head was used, and each step of circulation was prolonged to 24 h with a flowing rate of 15–20 ml/min. A passive incubation step of DCM for 6–8 h with gentle shaking was included before performing BABB-D10 circulation. Supplementary Table 1 summarizes the incubation times and temperatures of each clearing solution for whole-body clearing.

As a final note, the amount of solutions for circulation depends on the capacity of the clearing chamber. For mice whole-body clearing, if the maximum volume of the glass chamber is 400 ml, 300 ml of volume of solution was used for circulation. For rat whole-body clearing, a 1,000 ml capacity glass chamber with 800 ml working clearing solution would be sufficient.

PARS and CUBIC whole-body clearing methods (Fig. 1 and Supplementary Fig. 11) were performed following the original papers<sup>10,25</sup>.

**Vasculature labeling with Texas Red Dextran.** Texas Red Dextran (70,000 MW, Lysine Fixable, Invitrogen) was diluted in saline with a concentration of 15 mg/ml for mouse (0.1 ml per animal) and 8 mg/ml for rat (1 ml per animal). A pulled tubing (nonsterile polythene tubing, ID 0.86 mm, OD 1.27 mm, Harvard Apparatus) was attached to the syringe needle to achieve sharp ending thinner than femoral vein. For dextran injection, animals were anesthetized (MMF triple combination, 8 ml/kg, i.p.) and placed ventral side up. The right femoral vein was identified and exposed by surgical dissection in the inguinal region. The sharp ending of the tubing was inserted into the venous sinus of femoral vein, and the dextran was injected at a rate of 0.3–0.4 ml/min. After injection, the tubing was retreated and the wound was sealed by surgical suture. Then, the animals were placed in a warm cage for 15–20 min before proceeding with the standard perfusion and tissue preparation procedure. We experienced that skipping heparin in the pre-washing step of the perfusion (and using only 0.1 M PBS instead) resulted in better labeling of the vasculature.

**Neuronal tracing by AAV virus.** AAVs expressed EGFP (AAV2–Syn–EGFP) and RFP (AAV2–Syn–RFP) under the promoter of human Synapsin (Vector Core, University of North Carolina). The final titers were around  $2 \times 10^9$  GC (Genome Copy) per  $\mu$ l. For the virus injection, 3- to 4-month-old female C57BL/6N mice were anesthetized (MMF triple combination, 8 ml/kg, i.p.) and placed in a stereotaxic frame. To expose the motor cortex targeted for tracing axons into spinal cords, two cranial windows on each side of the skull were created within the area: 1.0 mm and 2.0 mm lateral; 0.5 mm anterior and 1.5 mm posterior to bregma. AAVs were injected into the cortex using a custom-established injector fixed with a pulled glass pipette. First, ten independent injection sites were targeted with the following coordinates: 1.2 mm and 1.8 mm lateral; 1.0 mm deep; 0.3 mm anterior to bregma, 0.1 mm, 0.5 mm, 0.9 mm, and 1.3 mm posterior to bregma. Next, 400 nl virus was injected at a rate of approximately 200 nl/min for every injection site. The glass pipette was kept *in situ* for 1 min before moving to the next site. After finishing all the injections, the cranial windows were covered by absorbable gelatin sponge (GELITA-SPON, GS-110), and the incision was closed by wound clips (CellPoint Scientific, part no. 203-1000). The animal was placed in a warm cage for waking up and then transferred into a regular keeping room. Carprofen (0.2 ml per injection, 1 mg/ml, i.p.) was given 3 times per d for 3 d. The animal survived for 4 weeks post virus injection before performing uDISCO.

**Culture and characterization of mouse BMSCs.** Mouse BMSCs were collected and cultured from  $\beta$ -actin EGFP mice as described previously<sup>32,48</sup>. Briefly, femur and tibia from 8- to 12-week-old mice (4–5 mice per culture) were removed under sterile conditions, and bone marrow was flushed out using a 20 gauge needle syringe. After mechanical dissociation with repeated flow of the bone marrow through needles of progressively smaller diameter, the cell suspension was filtered through a sterile 40  $\mu$ m nylon cell strainer mesh. Cells were resuspended in a final density of  $20 \times 10^6$  cells per ml of medium and were plated in T25

flasks (5 ml per flask) at 37 °C with 5% CO<sub>2</sub>. Culture medium was composed of aMEM, 10% lot-selected mesenchymal-stem-cell-qualified fetal bovine serum (FBS), 1% L-glutamine, 1% penicillin–streptomycin, and medium was stored at 4 °C for 1–3 weeks until usage. The medium was changed on day 2 (half of medium) and day 7 (complete change), followed by a complete change of medium every 3–5 d. Cells were passaged for the first time when 70–80% confluent using 0.05% trypsin–EDTA, and they were split at a 1:3 ratio.

Characterization of mix BMSCs was done with flow cytometry (FACS) and differentiation assays on passage 3. For FACS analysis the following primary antibodies were used in two different staining panels: CD11b-eFluor450 (eBiosciences 48-0112, clone M1/70, dilution 1:400), CD45.2-PE (eBiosciences 12-0454, clone 104, dilution 1:400), CD34-eFluor450 (eBiosciences 48-0341, clone RAM34, dilution 1:100), Sca1-APC (eBiosciences 17-5981, clone D7, dilution 1:200), CD29-PE (eBiosciences 12-0291, clone Hmb1-1, dilution 1:200), and CD44-APC (eBiosciences 17-0441, clone IM7, dilution 1:200). Briefly, cells were harvested by trypsinization with 0.05% trypsin, washed with ice-cold PBS, centrifuged at 1,500 r.p.m. for 8 min at 4 °C, resuspended at a concentration of  $1-5 \times 10^6$  cells/ml, and stained with the primary antibodies for 45 min at 4 °C in the dark. Following washing with ice-cold PBS three times, cells were immediately read at a flow cytometer (BD Biosciences, FACS Verse). Unstained cells and cells stained with the corresponding isotypic controls were used as negative controls for FSC, SSC, and autofluorescence adjustments.

Osteogenic and adipogenic differentiation capacity of BMSCs was tested on cells of passage 3 as previously detailed<sup>47</sup>. Bone mineralization and fat droplets after osteo- and adipo-differentiation were detected using alizarin red and oil red O staining assays, respectively, according to standard protocols. Chondrogenic differentiation capacity of mBMSCs was studied using the StemPro chondrogenesis differentiation kit (Gibco A10071-01) according to manufacturer instructions; proteoglycans produced by chondrocytes were stained with 1% alcian blue solution according to a standard protocol. Characterization of the transplanted EGFP+ mBMSCs is shown in Supplementary Fig. 19. Approximately 30% of the transplanted cells were EGFP+, and 60% were loaded with quantum dots.

**Labeling of cells with Qdots.** The EGFP+ BMSCs were cultured for 30–45 d until reaching passage 4 or 5. 1 d before transplantation, EGFP+ BMSCs were labeled with fluorescent carboxyl quantum dot nanoparticles (Qtracker Qdots, Invitrogen, emission at 655 nm or 800 nm). The nanoparticles were aseptically reconstituted according to manufacturer's instructions (20  $\mu$ l of component A and 20  $\mu$ l of B), allowed to sit at room temperature for 5 min, vortexed for 30 s, mixed with full BMSC medium up to a volume of 400  $\mu$ l, and then added to the flasks (200  $\mu$ l per 1 T75 flask with confluent BMSCs). Labeling of the EGFP+ BMSCs with Qdots 655 was checked 24 h later with microscopy and FACS analysis before transplantation. The efficiency of the labeling and the presence of any remaining free Qdots was also checked by sequential transferring of the Qdots-containing medium to a new flask with BMSCs, which did not produce any further cell labeling.

**Transplantation procedures.** Transplantation of the EGFP+ BMSCs, EGFP+/Qdot-labeled BMSCs, or vehicle (PBS) was

performed via tail vein intravenous (IV) or intraperitoneal (IP) injections. The injections were performed in C57BL/6N mice. All animals were food-starved overnight before the transplantation to clear the intestines for visualization.

For IV transplantation, animals were shortly anesthetized with 2% isoflurane. To achieve maximum vein dilation for successful infusion, the tail was shortly dipped and gently massaged in warm water (35–38 °C, for 10 s) and was then immediately placed for 5 min between a prewarmed (38 °C) heating pad and warm wet gauzes. The suspension of  $1 \times 10^6$  BMSCs in 300  $\mu$ l was injected IV at once using a 30-gauge needle attached to a 1 ml syringe. The injection caused a short heart arrest (approximately 10 s) in some animals that recovered either spontaneously or after short thoracic massaging. For IP transplantations, animals were briefly (30–60 s) anesthetized with isoflurane just before the injection and then received IP injection of  $1 \times 10^6$  BMSCs in 300  $\mu$ l of PBS at once. Following successful injections, animals recovered from anesthesia in a heat chamber (set at 30–31 °C) for approximately 30 min before returning to their home cage. The control animals were injected with PBS. 3 h after injection, we euthanized the animals for uDISCO.

**Imaging setup, light-sheet microscopy.** We used LaVision BioTec Ultramicroscope II light-sheet microscope (**Supplementary Table 2**). The axial resolution of the Ultramicroscope is 4  $\mu$ m, and the lateral resolution is 0.5–2  $\mu$ m, depending on the objective used (details are in **Supplementary Table 2**). We used exposure times of 250 ms to 50 ms, laser power of 1 to 3 mW (25% to 70% of the power level at a given wavelength, mostly centered around 470 nm, 545 nm, or 640 nm), distributed across a Gaussian light sheet of variable width and NA; according to the manufacturer specifications, the light sheet has a thickness of 4.5  $\mu$ m at its waist at 488 nm. A typical width spanning between 0.5 mm and 0.3 mm was chosen to adjust the illumination extent to the field of view of the objective used. The excitation branch of the imaging setup was used as provided, without further calibration. The microscope features a zoom body (Olympus revolving zoom unit U-TV, 1 $\times$ , 2 $\times$ , and 4 $\times$ ) equipped with an automated filter box for 25 mm mounted filters. An enhanced fluorescence acquisition branch consists of refractive-index-corrected long working distance objectives (Clear4brain, Munich): Olympus 2 $\times$ /0.15 NA (WD 10 mm), Olympus 4 $\times$ /0.28 NA (WD 10 mm) and Olympus 20 $\times$ /0.45 NA (WD 5 mm). Making use of the entire scanning area, defined by the built-in scanner capabilities, we acquired tile scans to cover the entire specimens.

**Imaging setup, laser-scanning confocal microscopy.** Cleared specimens such as brain slices or whole organs were incubated in BABB-D solution for a minimum of 2 h. Samples were mounted on histological glasses using transparent silicone gel (OBI, 4799656): a pool on glass was created with the glass as the bottom surface and silicone as walls, then samples were put into the pool filled with BABB-D. Eventually, glass coverslips were used to seal the pool, creating a closed chamber to prevent leakage of BABB-D.

Regions of brain slices were imaged with an inverted laser-scanning confocal microscopy system (Zeiss, LSM 880) using a 25 $\times$  water-immersion long working distance objective lens (Leica, 0.95 NA, WD = 2.5 mm) mounted on a custom mounting

thread. The z-step size was 3–5  $\mu$ m, and whole stacks of the slices were acquired (**Supplementary Table 2**).

**Imaging setup, fluorescence stereomicroscopy.** Cleared and uncleared specimens such as brain slices, whole bodies, or organs were immersed either in BABB-D or in PBS, respectively, and imaged with Zeiss AxioZoom EMS3/SyCoP3 fluorescence stereomicroscope using a 1 $\times$  long working distance air objective lens (Plan Z 1 $\times$ , 0.25 NA, WD = 56 mm; **Supplementary Table 2**).

**Image processing.** Processing and 3D rendering was executed by HP workstation with 8 core Xeon processor, 196 GB RAM, and Nvidia Quadro k5000 graphics card. We used Imaris, Amira, and Fiji (ImageJ2) for 3D and 2D image visualization. Stitching of tile scans was done via Fiji's stitching plugin<sup>49</sup>. Stitched images were saved in tiff format to enable fast processing using different software. We removed acquisition errors using Fiji's TrakEM2 plugin and Imglib2 (ref. 50) library.

Image processing consists of three main steps: error correction, image quality enhancement, and quantification.

*Error correction.* (e.g., **Fig. 3j**) Errors in image acquisition and following steps may occur for various reasons, such as physical interference with the microscope during image acquisition or miscalibration of a dynamic plate of the microscope, resulting in unwanted shifting of tiles or drifting effects between different slices of the same image series.

*Quality enhancement.* (e.g., **Fig. 5b**) We used filtering techniques (such as Gaussian, median, and anisotropic diffusion filtering) in the spatial domain for noise reduction. Morphological filters were used to correct the artifacts based on their shapes. Owing to the big size of data sets, filtering in the frequency domain is not feasible. Image intensity manipulation and equalization employed local (CLAHE in Fiji) and pseudo flat-field correction in Fiji (**Supplementary Video 1**).

*Quantification.* (e.g., **Fig. 5c**) To quantify the density of Qdot-positive BMSCs, we developed a simple workflow based on Fiji (**Supplementary Fig. 29**).

**Quantifications.** *Normalized fluorescence signal profile plots and total signal intensity.*

Normalized signal profiles demonstrate the quality of the signal over the background, which defines the ability to trace the individual cellular structures in the scans (e.g., axon tracing in **Supplementary Video 6**). We calculated the total signal intensity to compare the remaining fluorescence signal after each clearing method. We presented details of these calculations with example images in **Supplementary Fig. 30**.

For normalized signal profile measurement, a straight line was drawn across the specific area, which includes signal and background, and plotted via Fiji's 'plot profile' option. To calculate the mean background intensity, we chose another line adjacent to the profile line with no intersection to any specific signal. Subsequently, the profile plot was normalized by dividing the profile data over the calculated mean background intensity. Normalized profile of each sample was shown in the representative line chart (**Supplementary Figs. 2,5,6 and 10**).

For total signal intensity quantification, we selected a rectangular area covering the signal (several cellular structures), and measured the integrated density as the representative of the total signal

intensity of selected area. To calculate the mean background, a straight line was drawn across the area. Eventually, the total sum of the signal intensity in the sample area was determined as:

$$\begin{aligned} \text{Sum of background intensity} &= \text{Number of background pixels} \\ &\quad + \text{Mean background value} \\ \text{Sum signal intensity} &= \text{Total sum of intensity of the area} - \text{Sum} \\ &\quad \text{of background intensity} \end{aligned}$$

We calculated the average total signal intensity by dividing the sum of the signal intensity over the pixel number of the rectangular selection (**Supplementary Figs. 2,5,6,9 and 10**).

*Signal-to-noise ratio (SNR)*. A small part of the image was selected, and pixels belonging to a specific signal were separated from the background by thresholding the input image,  $f$ , and applying the binary image as the mask to the same image.

$$\begin{aligned} f(n,m) &= S(o,p) + X(i,j) \\ o &\neq i, p \neq j \end{aligned}$$

$S$  is the image that contains only the specific signal, and  $X$  is the background image. SNR was calculated based on Jahr *et al.*<sup>51</sup>

$$\text{SNR} = \text{Mean}(S) / \text{Std}(X)$$

*Peak signal-to-noise ratio (PSNR)*. PSNR was calculated as previously described<sup>52</sup>. In brief, we used a mean square error (MSE) calculation between the sample image and a reference image. We took the average intensity of the background pixels as the reference image without the noise. Then, we calculated the MSE and PSNR as:

$$\text{MSE} = \frac{1}{N * M} \sum_{i=0}^{N-1} \sum_{j=0}^{M-1} [X(i,j) - Y(i,j)]^2$$

$Y$  is the reference image with  $N \times M$  dimension.

$$\text{PSNR} = 20 * \log_{10} \left( \frac{\text{MAX}}{\sqrt{\text{MSE}}} \right)$$

$\text{MAX}$  represents the maximum intensity of the input image  $f$  in the selected neighborhood.

*RMSE calculation*. The root mean square (RMS) of the morphology deformation error at single-cell scale was used as a quantification factor for isotropy. RMSE calculation includes three steps: 1) Postclearing and preclearing images of a single cell were registered by similarity transformation in Fiji's TrakEM2 plugin. To achieve perfect overlay, output images from step 1 were registered with nonrigid transformations using Fiji's bUnwrap plugin<sup>53</sup>. 2) The deformation parameter for preclearing image pixels was masked with a skeletonized preclearing image to remove irrelevant deformation parameters. 3) RMS of the deformation error with respect to the distance from the center of the cell or vessel (constant point) was calculated<sup>37</sup>.

*Fluorescence level*. Fluorescence level quantification was expressed as a signal-to-background ratio and was calculated using Fiji at the following timepoints after clearing: 0, 4, 7, 19, and 37 d (**Fig. 1b**). From each brain scan, a  $z$ -projection of three consecutive images in Tiff format was made at the same anatomic region for all the samples. The mean value of the background for each  $z$ -projection was obtained by averaging the background

values of 15–20 regions from equally sized areas of the projection without signal. To calculate the mean value of the signal of each  $z$ -projection, we used the threshold function of the software; the threshold was adjusted to consider the fluorescence signal visible in the projection. After adjusting the threshold, only the sharp signal from specific cellular structures was analyzed per each  $z$ -projection. To this end, we used Fiji's "analyze particles" to measure the signal intensity only of particles sized between 10 and 150 pixels (visible fluorescent cells), and we calculated the mean value from all the particles. Next, this value was divided by the mean value of the background of the respective projection, obtaining the fluorescence level on the background.

*Imaging depth quantification*. To assess the imaging depth between different clearing methods (CUBIC, PARS, PACT, and uDISCO), the tile scans of three whole brains per clearing method were taken with a light-sheet microscope with 4  $\mu\text{m}$   $z$  step (in **Fig. 1h,i**, and **Supplementary Fig. 11**). 3D reconstructions at the same anatomic level (from the surface of the brain to the center of the brain, including the region of the hippocampus) of each sample were shown in the coronal view using Imaris. Next, the images of the 3D reconstructions were analyzed in Fiji. Using the scale bar provided by Imaris, the distance of imaging depth was measured from the surface (where the signal was sharp) to the inner part of the brain until the last identifiable signal over the background coming from cell body or cellular structure (e.g., axons or dendrites) was detected.

**Statistical analysis**. Data are presented as mean  $\pm$  s.d. in **Figs. 1b–d,h,i;3i;6h,n** and in **Supplementary Figs. 4,7b,8c,11b,12e,13s,25i,26**. Data are presented as mean  $\pm$  s.e.m. in **Fig. 5c** and in **Supplementary Figs. 2c,5h,6h,9g,10h**. The data distribution in each experiment was checked for normality using Shapiro–Wilk test in IBM SPSS statistics software.  $P$  values were calculated using unpaired  $t$ -test to compare data between two groups (**Supplementary Figs. 2c,4,8c,25i**). One-way ANOVA was used to compare more than two groups of data (**Fig. 1b–d,h,i**; and **Supplementary Figs. 5h,6h,9g,10h,11b,12e,13s**); if ANOVA was significant, it was followed by *post hoc* Dunnett's test for multiple comparisons (**Figs. 1b–d,h,i** and **Supplementary Figs. 5h,6h,9g,10h,11b**).

44. Pan, C., Cai, R., Quacquarelli, F.P., Ghasemi, A. & Ertürk, A., Whole organ and organism tissue clearing by uDISCO. *Protocol Exchange* (2016).
45. Kilkenny, C., Browne, W.J., Cuthill, I.C., Emerson, M. & Altman, D.G. Improving bioscience research reporting: the ARRIVE guidelines for reporting animal research. *PLoS Biol.* **8**, e1000412 (2010).
46. Acar, M. *et al.* Deep imaging of bone marrow shows non-dividing stem cells are mainly perisinusoidal. *Nature* **526**, 126–130 (2015).
47. Ertürk, A., Lafkas, D. & Chalouni, C. Imaging cleared intact biological systems at a cellular level by 3DISCO. *J. Vis. Exp.* **89**, e51382 (2014).
48. Zacharakis, D. *et al.* Characterization of *in vitro* expanded bone marrow-derived mesenchymal stem cells isolated from experimental autoimmune encephalomyelitis mice. *J. Mol. Neurosci.* **51**, 282–297 (2013).
49. Preibisch, S., Saalfeld, S. & Tomancak, P. Globally optimal stitching of tiled 3D microscopic image acquisitions. *Bioinformatics* **25**, 1463–1465 (2009).
50. Pietzsch, T., Preibisch, S., Tomancak, P. & Saalfeld, S. ImgLib2—generic image processing in Java. *Bioinformatics* **28**, 3009–3011 (2012).
51. Jahr, W., Schmid, B., Schmied, C., Fahrbach, F.O. & Huiskens, J. Hyperspectral light sheet microscopy. *Nat. Commun.* **6**, 7990 (2015).
52. Gonzalez, R. *Digital Image Processing* 3rd edn. (India, Pearson Prentice Hall, 2006).
53. Arganda-Carreras, I. *et al.* Consistent and elastic registration of histological sections using vector-spline regularization. in *Computer Vision Approaches to Medical Image Analysis* (eds. Beichel, R.R. & Sonka, M.) 85–95 (Springer, 2006).

